The Toroidal Slit Energy-Dispersive Diffractometer at CHESS

Arthur R. Woll[1], Christopher J. Budrow[2], Joseph A. Crum[1], Amlan Das[1], J.Y. Peter Ko[1] and Kelly E. Nygren[1,3]

[1]Cornell High Energy Synchrotron Source, Cornell University, Ithaca, NY USA

[2]Budrow Consulting, Loudonville, NY USA

[3]Sibley School of Mechanical and Aerospace Engineering, Cornell University, Ithaca, NY USA

E-mail: arthurwoll@cornell.edu

Abstract. We describe the design and performance of a novel instrument for energy dispersive X-ray diffraction (EDXRD). The instrument, coined a toroidal slit diffractometer (TSD), is based on a 23-element germanium detector with elements arranged in a semicircle and two pairs of variable-gap semicircular slits made from 6.6-mm thick tungsten plates. The working surfaces of the slits form a toroidal surface, permitting tunable scattering angle from 5 to 9°and tunable slit size from <0 to 3 mm in the radial direction. The TSD was commissioned in the fall of 2023 at the Structural Materials Beamline (SMB) at the Materials Solutions Network at CHESS (MSN-C) for use with wiggler radiation spanning 40-200 keV. Here we describe the design features and performance of the TSD. We show that its key performance metrics, namely the uniformity of gauge volume size and position, are precisely accounted for by laser-based metrology of the four slits. We then highlight the performance of the new instrument by comparing strain maps obtained from nearly identical Ni-based superalloy samples using the TSD and the single-element system previously employed at SMB.

1 Introduction

Energy-dispersive X-ray diffraction (EDXRD) [1–4] employs a broad-energy-band incident beam, fixed Bragg angle, and collimating slits both up- and downstream of the sample position to obtain diffraction from a finite 3D region within a sample (see inset of Figure 1a). The combination of instrument-defined 3D probe volume, small Bragg angle (typically <10°) and X-ray energies up to 300 keV [2] permits diffraction-based analysis of thick, complex-shaped parts not amenable to conventional XRD using monochromatic beam and an area detector. These advantages are particularly important for challenges related to the design and manufacture of structural metallic components used in aerospace and other applications.

Since 2019, the Structural Materials Beamline (SMB) at the Materials Solutions Network at CHESS (MSN-C) has provided EDXRD for elastic strain mapping using the conventional geometry [1, 2] comprising a single-element germanium detector and two pairs of collimating slits. Although this capability is in high demand [5], its throughput is limited by the common necessity of long collection times (e.g. for thick samples) and the fact that only one normal strain can be probed at a time.

To overcome this limitation, several facilities have developed multi-element detector approaches to EDXRD. To our knowledge these include 2-element systems based at BESSY-II [3, 4] and the APS [6], a 10-element system at the APS [6], and a 23-element system at DLS [7]. The success of such efforts

and increasing demand for EDXRD from SMB's structural materials-based user community motivated development of a new EDXRD system at CHESS. The system, shown in Fig. 1a, employs the same 23-element detector geometry as that in [7], but with a novel, custom slit system described below. In contrast to the collimating systems employed in the 10- and 23-element setups referred to above, these slits provide easy, continuous tuning of the gauge volume and scattering angle, enabling the TSD to be optimized for particular materials or components. Here, we show that the performance of these slits for EDXRD is accurately predicted on the basis of laser metrology carried out prior to assembly. In addition, we demonstrate the performance of the TSD system as a whole by comparing strain maps on nearly-identical samples obtained using the TSD and our previously-deployed single-element setup.

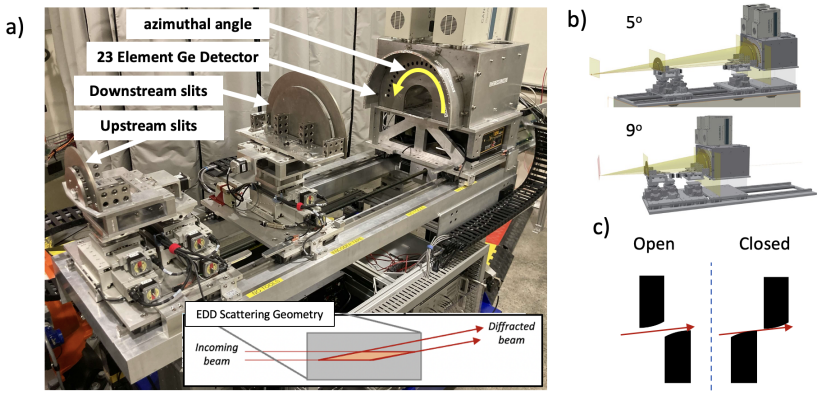

Figure 1: (a) Photograph of the TSD with labels for the 23-element detector as well as the the up- and downstream toroidal slit pairs; (b) CAD-generated schematics of the TSD illustrating motion of the three labeled components in (a) when changing between scattering angles; (c) Schematic representation of how counter-translation of each pair of slits results in variation of their effective gap.

2 Diffractometer Design

Figure 1a shows the TSD installed on its custom optical table (AVS | US, USA) in the SMB hutch at CHESS highlighting the two slit assemblies and detector. The 23 elements of the detector (Mirion Technologies, USA) are cylindrical germanium diodes with an active area and thickness of 200 mm^2 of 13 mm, respectively, arranged at equally-spaced angular intervals around a 175.0 mm-radius circular arc spanning 180°. The detector employs thermoelectric cooling, enabling the detector to remain cold when not in use without the need to refill liquid nitrogen, thus reducing the frequency with which the detector is thermally cycled between room temperature and its operating temperature of -180°C. Such thermal cycling is known by the manufacturer to gradually deteriorate the electrical contacts on the detector elements, which in turn contributes to electrical noise and loss of energy resolution. Background reduction is achieved in part by a detector enclosure made of 6.4-mm lead panels in addition to a 25.4-mm steel front plate with machined apertures for each detector element. An Xspress 3X signal processor (Quantum Detectors, UK) is used to digitize and process each detector element output into spectra.

The two pairs of slits are made from 6.6-mm thick, half-disk-shaped tungsten plates. In order to achieve the target performance (described further below), the four active slit surfaces were cut using electrical discharge machining (EDM) (Swiss Wire EDM, USA), which can routinely achieve tolerances as low as ± 5 μm. Schematic illustration of the cross sections of these plates are shown in Figure 1c. Each of the (toroidal) active surfaces is formed by rotation of a convex arc around an axis coinciding with the incident beam. The meridional angle, defined as the angle between the active surface and incident beam, was designed to vary from 5 to 9°. Figure 1c also illustrates that each slit opening is controlled by counter-translation of the inner and outer plates. This translation is accomplished for each pair of slits using a single dual-thread lead screw and permits gap variation from <0-3 mm. The precise value of this gap at a given slit position varies slightly with scattering angle, but may be precisely determined and selected using scans such as those represented in Figs. 3a and c, described below.

The two slit assemblies and detector are mounted on a shared pair of precision rails. Six degrees of freedom on the table permit the translation axis defined by these rails to be precisely aligned to the incident beam. Additional degrees of freedom permit precise lateral and angular alignment of each slit

assembly. Figure 1b illustrates how collective motion of the three carriages permits dynamic selection of the scattering angle from 5 to 9 degrees maintaining constant sample position. The mean radii of the up- and downstream slit pairs are 71 mm and 169 mm, respectively, resulting in a large working distance, $\geq$440 mm, between the probe volume upstream slit assembly.

3 Results

3.1 Laser-Based Slit Metrology

Two key performance metrics of any multi-detector system for EDXRD are the uniformity among the sizes and locations of the gauge volume measured by each detector [6, 8]. For the system described here, both metrics are determined by the variation of the radii $R(\eta)$ of the four slit surfaces as a function of azimuthal angle η (see Fig. 1a).

Prior to assembly, metrology of each slit was undertaken using a laser-based profiler (Keyence model LJ-X8080), which employs line-like laser emission to simultaneously measure 3200 heights with sub-μm accuracy across a lateral distance of up to 39 mm. Measurements were prepared by mounting each slit on a heavy duty goniometer stack on top of a rotation stage (see Figs. 2a and b), and aligning their axes of revolution with the rotation axis of the bottom stage to $\pm$0.002 μm. Once aligned, the rotation stage was scanned by 190 degrees while obtaining a 1D height profiles at 0.56°intervals. Thus, a single angular scan results in a complete, 2D measurement of the active surface [9].

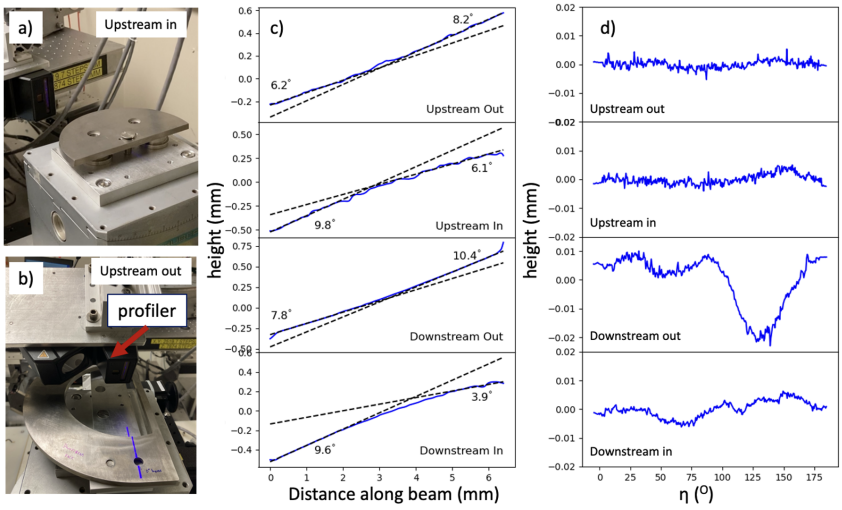

Figure 2: (a-b) Metrology setup for the (a) upstream inner and (b) upstream outer slit; (c) Meridional projections of each of the four slit surfaces averaged from 80-100°in η; (d) Azimuthal projections of each of the four slit surfaces averaged from 2.5-4 mm in meridional direction. The vertical scale of each plot in (d) are equivalent to aid visual comparison among the different slits.

Figures 2c and d show projections of the measured heights of each active surface, projected in (c) along the meridional (thickness) dimension, and in (d) along the azimuthal direction. The positive y axes in both (c) and (d) correspond to the outward radial direction from the center of revolution for each slit, such that in (c) the outer surfaces curve up and the inner slits curve down. The measurements show conspicuous differences from the design shape, but that the convexity is preserved on each slit.

Figure 2d, which shows an azimuthal projection of each of the four slits, reveals remarkable uniformity in radius for three of the four slit surfaces. Specifically they show rms variation of $<$5 μm in all cases except for the inward facing surface of the downstream slit pair, which exhibits a 25$\pm$2 μm asperity centered near $\eta = 135°$. Because that slit faces inward, this high point on the slit surface appears as lower values along the y axis on the plot. As demonstrated below, this asperity manifests in the TSD in both the size uniformity of the downstream gap as well as the position of the gauge volume.

3.2 Slit Performance Determined by X-rays

Initial commissioning of the TSD was performed with monochromatic beam (E=61.33 keV) incident on a 1-mm thick CeO_2 powder sample sandwiched in kapton tape. Alignment is evaluated by scanning the

sample position along the incident beam as in Fig. 3e (described further below), and is achieved when the deviation in peak position and intensity is minimized. Subsequent to commissioning, TSD alignment takes between 1 and several hours depending on its prior state. All 23 detector elements were found to achieve specified energy resolution, varying from 380 to 650 eV (FWHM) in the energy range of 40-140 keV. However, unanticipated characteristics of the detector signals and signal processor, for instance cross-talk among the detector signals, resulted in only 16 of the 23 elements being initially usable.

Once aligned, the two key performance metrics of the TSD enumerated above were determined directly using diffracted intensity from the 311 Bragg Peak of CeO_2 at a scattering angle of 7.106°. First, gap uniformity was measured by scanning each slit gap through their closed positions. Figures 3a and c show data obtained from scans of the upstream and downstream slit gaps, respectively, from each of the 16 detector elements in use. The x-intercept of each plot indicates the true "closed" position for the section of the slit in front each corresponding detector element. The variation of these positions, subtracted by their average, are plotted as solid blue lines in Figs. 3b and d. This variation in gap can also be calculated directly from the data in Figure 2d. More specifically, the red lines in 3b and d are calculated as the difference between the data in each pair of plots of 2d (the upper two for 3b and lower two plots for 3d). These differences are then averaged over 6°regions in η spaced 8.18°apart to correspond, approximately, to the angular acceptance of each detector element.

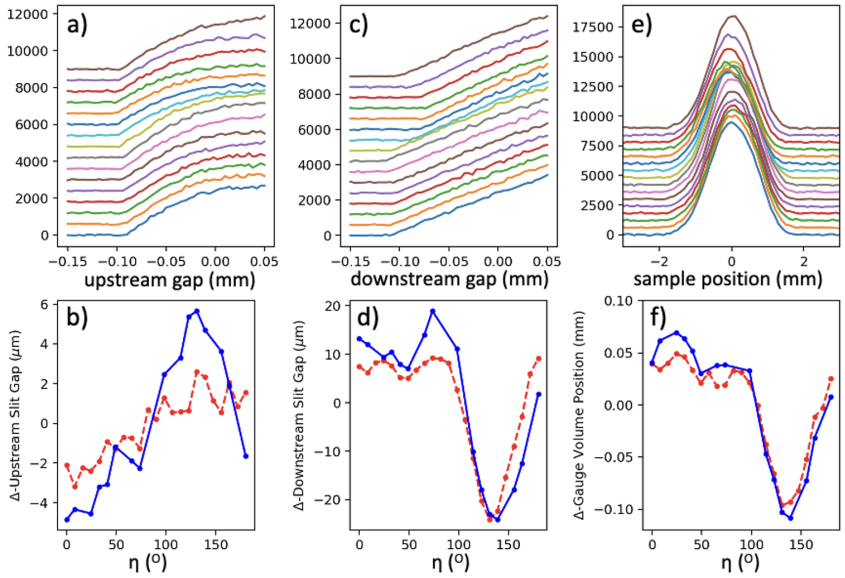

Figure 3: (a) X-ray intensity vs. nominal gap of the upstream slit assembly on 16 of 23 detector elements, offset for clarity; (b) Comparison of variation in upstream slit gap vs. η determined (blue solid line) from the x-intercepts of the data in (a) and (red dashed line) from the data represented in figure 2; (c), (d) Like (a) and (b) but for the downstream slit assembly; (e) Scan of a 1 mm thick CeO_2 powder sample through the gauge volume along the beam direction; (f) Comparison of variation in gauge volume center vs. η as measured in (e) with a calculation of this variation based on the data in figure 2 as described in the text.

As expected from the metrology results in Figure 2d (3rd plot from the top), the height asperity on the downstream, inward-facing slit surface results in a commensurate, 25-30 μm decrease in the gap near $\eta = 135°$. On the other hand, Figs. 3b and d show that for both the whole of the upstream slit as well as the downstream slit away from the region affected by this defect ($0 < \eta < 100°$), the gap size variation is just ± 4 μm.

The second key performance metric determined strictly by the slits, namely variation in probe volume position along the incident beam, is determined by scanning a thin sample through the probe volume and observing deviation in peak position among all detectors. One such scan of the 1-mm thick CeO_2 powder sample is shown in Figure 3e. The peak positions of each curve were determined as the average of intensity-weighted scan positions after background subtraction. As in Figures 3b and d, these positions, subtracted by their mean, are plotted as a blue solid line in Figure 3f, and reveal a position shift of 160 ± 20 μm near $\eta = 135°$corresponding to the location of the defect in the inner downstream slit surface.

To compare this result to the metrology in Figure 2d, we first compute the variation of centers of the upstream and downstream gaps as a function of η by averaging the data in the upper pair of plots for the upstream slit and the lower pair of plots for the downstream slit, then subtracting their mean. The resulting values, $\Delta R_{\text{up, down}}(\eta)$, are then added to the nominal radii R of each slit, namely 71 and 169 mm, resulting in the actual radii $R_{\text{cen: up, down}}(\eta)$, corresponding to the distance from the incident beam to the the center of each slit as a function of η. For each value of η, rays that intersect these center positions are then extrapolated back the path of the incident beam. The position of intersection between these rays and the incident beam is the calculated gauge volume position as a function of η, shown as the red dashed line in 3f.

Considering the totally independent nature of the laser- and X-ray-based measurements and absence of free parameters, we consider the agreement shown in Figures 3b, d, and f to be very good. The significance of this agreement is to show that laser metrology can be reliably employed to characterize toroidal slit performance prior to assembly. Replacement of the downstream inner slit is anticipated in early 2025. Based on the metrology shown above, we anticipate replacement of this slit to improve the variability in gauge volume *size* from ± 20 μm to ± 4 μm, (commensurate with the variability observed for the upstream slits shown in Fig. 3b) and the variability in gauge volume *position* from 160 ± 20 μm to as little as ± 15 μm.

3.3 Diffractometer Performance for EDXRD

As a first test of TSD performance, data were obtained on an additively-manufactured (AM) sample made from the Ni-based superalloy Inconel 718. The sample was produced for the NIST-led "AM Bench" project [10, 11], which aims to provide rigorous, benchmarked residual strain data for the purpose of validating predictive models of the AM process. Improving such models is a critical step towards improving prediction and mitigation of residual stress in AM manufactured components [12], which currently limits their wider application. The sample, shown in Fig. 4a, is $75 \times 12 \times 5$ mm^3 in extent and incorporates a sequence of bridge-like features designed to result in residual stress. A nearly identical sample was previously measured using the single-detector configuration previously employed at the SMB beamline.

Figures 4b and c compare the residual strains from the two samples described above obtained using the single element configuration (Fig. 4b) and the TSD (Fig. 4c). For the data in Fig. 4b, the incident beam dimensions were 0.2×0.4 mm^2 and the collimating slits were set to 0.2×1.0 mm^2. For Fig. 4c, the incident beam as 0.2×0.2 mm^2 and the toroidal slit gaps were each set to 0.2 mm. In both cases, the scattering angle was 8°, the samples were mounted with their 75×12 mm^2 faces perpendicular to the beam, and the 3D gauge volume was aligned to the mid-plane of the 5-mm thickness dimension. Figure 4b represents data collected from 2248 scan positions with a dwell time of 60 seconds. The point spacing was decreased in the region away from the bridge features to reduce total scan time. The data represented by Fig. 4c were collected from a larger number of sample positions, 4000, and a shorter dwell time of only 10 seconds per position.

Figures 4b-c suggest that the two data sets yielded very similar results, despite the factor-of-six decrease in dwell time for data collected using the TSD. Considering the additional gain represented by the data from the 15 additional detector elements collected simultaneously with the data represented in Fig. 4c, the TSD represents a two-order-of magnitude gain in the data obtained per unit time.

4 Summary and Outlook

In this paper we have described a novel instrument for EDXRD based on a 23-element detector and a novel variant of conical slits. In contrast to prior implementations of multi-element EDXRD, our design permits motorized variation of slit gap and scattering angle, enabling fast optimization of these parameters to suit different materials and/or components. We showed that the key performance metrics of the system can be well understood using metrology of the slit surfaces, and demonstrated that the TSD represents a 2-order of magnitude increase in measurement efficiency compared to our previously-deployed single-element system. The scale of this increase in efficiency significantly widens the scope of EDXRD applications to: calculation of a full strain tensor within one or more 3D sub-volumes of a sample, high-spatial resolution maps of residual strain, measurement of residual strain on large, near-net-shape components, insights into crystallographic texture, and combinations of the above. Beyond structural materials, this approach may impact other scientific domains that commonly employ EDXRD, especially high pressure science [6] and *in operando* studies of batteries [13] or other functional devices.

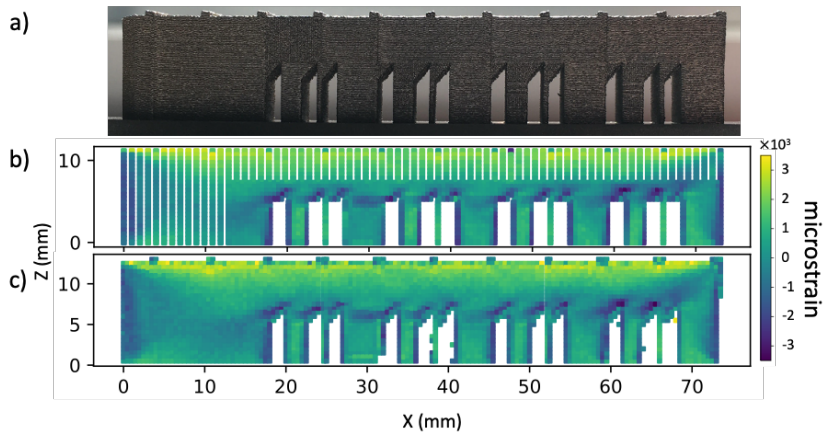

Figure 4: (a) Photograph of the AM Bench bridge sample used to evaluate TSD performance for EDXRD. (b,c) Residual strain (ε_{xx}) in the sample in (a) measured using the (b) single element detector and (c) the TSD. The veritical white features in (b) reflect the lower-density of scan points obtained in those regions with the single-element detector, in order to reduce scan time.

5 Acknowledgements

This material is based on research sponsored by AFRL under agreement number FA8650-22-2-5200. The authors thank MSN-C programmer and analysts Keara Soloway and Rolf Verberg for their many contributions to data analysis pipelines for EDXRD, as well as the CHESS technical staff for their many contributions relating to design and fabrication of the TSD shielding enclosure, control system, assembly and commissioning. We especially acknowledge John Kopsa, Jessica Turco, John Dobbins, Seth Bywater, Eric Edwards, Ryan Ford, and Kyle Brogan. We also thank Darrel Lane (Swiss Wire EDM), Wilhelm Mueller and Jim Evans (Mirion Technologies) and Rachel Ash, Oliver Sargent, and Tom Griffin (Quantum Detectors) for their dedication and support, and Darren Pagan (Penn State) for leading initial specification and purchase of the 5-element version of this detector for EDXRD. Finally we thank Mark Obstalecki, Paul Shade (AFRL) and Basil Blank (PulseRay) for executing the 5- to 23-element detector upgrade, and Professor Matt Miller (Cornell University) for critical discussions.

References

1. Croft, M. *et al. J. Appl. Phys.* **92,** 578–586 (2002).
2. Steuwer, A. *et al. J. Appl. Crystallogr.* **37,** 883–889 (2004).
3. Genzel, C. *et al. The J. Străin Anal. for Eng. Design* **46,** 615–625 (2011).
4. Apel, D. *et al. Nuclear Instruments Methods Phys. Research Sect. A: Accel. Spectrometers, Detect. Assoc. Equip.* **877,** 56–64 (2018).
5. Fisher, C. R. *et al. J. Manuf. Process.* **74,** 75–87 (2022).
6. Park, J. S. *et al. Exp. Mech.* **62,** 1363–1379 (2022).
7. Drakopoulos, M. *et al. J. Synchrotron Radiat.* **22,** 828–838 (2015).
8. Weidner, D. J. *et al. Review Sci. Instruments* **81,** 013903 (2010).
9. CHESS Data Provenance: Laser metrology: 2023-1/id3b/woll-keyence-0; Slit Characterization: 2023-3/id1a3/ko-3538-a/edd23-char-1; AM Bench single-element data: 2021-3/id1a3/phan-3033-b/Sample-d-map-x;AM Bench TSD data: 2023-3/id1a3/yeung-3714-b/v8-p3-10s-0deg.
10. Phan, T. Q. *et al. Integrating Mater. Manuf. Innov.* **8,** 318–334 (2019).
11. Levine, L. *et al. Integrating Mater. Manuf. Innov.* **13,** 598–621 (2024).
12. Li, C. *et al. Procedia CIRP* **71,** 348–353 (2018).
13. Marschilok, A. C. *et al. Phys. Chem. Chem. Phys.* **22,** 20972–20989 (2020).